Orbital- and atom-dependent linear dispersion across the Fermi level induces charge density wave instability in $EuTe_4$

Abhishek Pathak,[1] Mayanak K. Gupta,[2] Ranjan Mittal,[2,3] and Dipanshu Bansal[1,4,*]

[1]*Department of Mechanical Engineering, Indian Institute of Technology Bombay, Mumbai MH 400076, India*

[2]*Solid State Physics Division, Bhabha Atomic Research Centre, Mumbai MH 400085, India*

[3]*Homi Bhabha National Institute, Anushaktinagar, Mumbai MH 400094, India*

[4]*Center for Research in Nano Technology and Science, Indian Institute of Technology Bombay, Mumbai MH 400076, India*

(Received 3 September 2021; revised 23 December 2021; accepted 3 January 2022; published 13 January 2022)

In the Peierls description of a charge density wave (CDW), Fermi surface nesting (FSN)—defined by the divergence of the imaginary part of electronic susceptibility, i.e., $\mathrm{Im}\{\chi_0\}$—leads to divergence of the real part, thus inducing CDW instability at wave vector $\mathbf{q}_{\mathrm{CDW}}$. Here we show that the divergence of $\mathrm{Im}\{\chi_0\}$ implying a divergence of $\mathrm{Re}\{\chi_0\}$ at the same $\mathbf{q}_{\mathrm{CDW}}$ breaks down for three-dimensional Fermi surfaces and is particularly severe for linearly dispersing electronic bands across the Fermi level (E_{F}), as exemplified by rare-earth tellurides $R\mathrm{Te}_n$. By calculating the orbital-, atom-, and momentum-resolved contribution to χ_0 of $EuTe_4$, we find that FSN and CDW instability are not driven by the same atoms and orbitals but from different ones. This unique behavior is enabled by linearly dispersing bands across E_{F} with constant Fermi surface velocity that assists electron-hole pairs to form not only at E_{F} but also across E_{F} at $\mathbf{q}_{\mathrm{CDW}}$, hence allowing different orbitals to contribute to the divergence of $\mathrm{Re}\{\chi_0\}$ and $\mathrm{Im}\{\chi_0\}$. The above scenario is general and applicable to recent observations of CDWs and spin density waves (SDWs) from linearly dispersing bands in several Dirac and Weyl semimetals and kagome metals. Moreover, as we demonstrate, such component-resolved analysis provides focused input to engineer CDW and SDW states.

DOI: 10.1103/PhysRevB.105.035120

A charge density wave (CDW) leads to a periodic spatial modulation of the charge density in metals, thus creating collective electronic condensates below the CDW transition temperature T_{CDW} [1,2]. Rare-earth tellurides, $R\mathrm{Te}_n$, are particularly interesting as the entire family shows CDW ordering at an easily accessible temperature of the order of 100 K, where $n = 2$, 3, and 4 [3–17]. Despite CDWs occurring in inherently unstable square-net Te plane(s) for all n [18], the origin of a CDW is vastly different. For $R\mathrm{Te}_2$, diffraction and angle-resolved photoemission spectroscopy (ARPES) showed that Fermi surface nesting (FSN) induces CDWs [4,5]. On the other hand, for $R\mathrm{Te}_3$, the CDW mechanism is still being debated. ARPES measurements on $R\mathrm{Te}_3$ found (imperfect) FSN induces CDW distortion [8], while inelastic x-ray spectroscopy (IXS) of two different rare earths, $TbTe_3$ and $DyTe_3$, proposed *wave-vector-dependent* electron-phonon interaction (EPI) to be the governing mechanism [11,12]. Another critical distinction between $R\mathrm{Te}_2$ and $R\mathrm{Te}_3$ is the spectral band gap of the entire Fermi surface, which is fully gapped for $LaTe_2$ [4], but residual metallic pockets are visible for all measured $R\mathrm{Te}_3$ [7,8].

The structures for all n are composed of corrugated $R\mathrm{Te}$ slabs separated by monolayer and/or bilayer Te planes. For $n = 2$, 3, and 4, stacking patterns perpendicular to the Te planes follow: $(R\mathrm{Te})_2{-}\underline{\mathrm{Te}}{-}\cdots$, $(R\mathrm{Te})_2 - \overline{\mathrm{Te}} - \overline{\mathrm{Te}} - \cdots$, and $(R\mathrm{Te}) - \overline{\mathrm{Te}} - \overline{\mathrm{Te}} - (R\mathrm{Te}){-}\underline{\mathrm{Te}}{-}\cdots$, respectively. Here an underline and an overline imply Te atoms in mono- and bilayers, and $\cdots$ implies that stacking previous to the dots is repeated (see Fig. 1). R is trivalent in $n = 2$ and 3 series, which fill the Te p orbitals within the slab and donate one electron to partially fill p orbitals in the Te planes. On the contrary, R is divalent in $n = 4$, and it does not accept or donate any electrons to the Te planes, thus the Te planes remain nominally neutral [17]. Notably, an extra monolayer in $R\mathrm{Te}_4$ provides an additional degree of freedom for an equilibrium CDW state as the relative phase difference of CDW distortion (ϕ) between the adjacent Te bilayer and Te monolayer can be 0 (in-phase) or π (out-of-phase). However, for both $R\mathrm{Te}_3$ and $R\mathrm{Te}_4$, ϕ is symmetry-constrained within the Te bilayer. These symmetry-allowed in- and out-of-phase CDW distortions are separated by a large energy barrier of the order of eV, and they underlie a record ~400 K hysteresis in recently synthesized $EuTe_4$ [16,17]. Moreover, compared to partially gapped states in $R\mathrm{Te}_3$, $EuTe_4$ harbors a fully gapped CDW state in the $(H, K, 0)$ scattering plane with $E_g \approx 0.2$ eV [17]. These important distinctions of $R\mathrm{Te}_4$ from others in the $R\mathrm{Te}_n$ family raise intriguing questions about the origin of CDW distortion in charge-neutral monolayer and bilayer Te planes and its implications on electronic band renormalization leading to a gapped state in $EuTe_4$.

Several mechanisms of CDW distortion, supported by both measurements and simulations, are identified in the literature, including FSN and hidden nesting [1,2,19–23], wave-vector-dependent EPI [11,12,24,25], strong electron correlations [20,26,27], and large electronic density of states

*dipanshu@iitb.ac.in

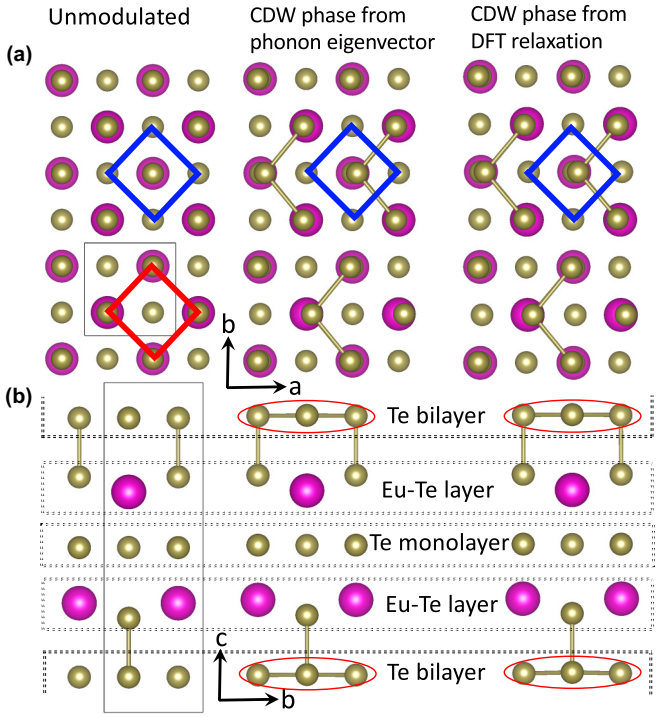

FIG. 1. (a), (b) Crystal structure of unmodulated and CDW state of $EuTe_4$ in *a*-*b* and *b*-*c* planes. Red and blue squares indicate the Te square lattice in Te bilayer and monolayer planes, respectively. Naming of Te layers is shown in panel (b). CDW state is obtained from freezing the unstable phonon eigenvector (middle column) and by relaxation of atomic coordinates using DFT (right column). Te atoms form trimers in the Te bilayer in the CDW phase. All bonds shown between Te atoms are shorter than 2.97 Å.

(EDOS) near E_F in high-symmetry structures with degenerate branches [28,29]. To unambiguously identify the governing mechanism, we must confirm the CDW's signatures in both electronic $\chi_0(\mathbf{q}, \omega)$ and lattice $\chi_L(\mathbf{Q}, E)$ susceptibilities. Here $\mathbf{q}$ is the reduced wave vector, ω is the external perturbation frequency, $\mathbf{Q}$ is the momentum transfer, and E is the phonon energy.

In this paper, we investigate atom-, orbital-, and momentum-resolved $\chi_0(\mathbf{q}, \omega)$ and $\chi_L(\mathbf{Q}, E)$ to identify the governing mechanism of a CDW. We find that the FSN and electronic instability, which are given by divergence of the imaginary (Im) and the real (Re) part of $\chi_0(\mathbf{q}, \omega)$, respectively, do not arise from the same electronic bands and instead originate primarily from Te bands in Te monolayer and bilayer. Importantly, without separating the contribution of $\chi_0(\mathbf{q}, \omega)$ into different orbitals of various atoms, the mechanism is reminiscent of Peierls' description of a CDW in an ideal one-dimensional monatomic chain [30,31], where the same bands lead to divergence of both $\mathrm{Im}\{\chi_0(\mathbf{q}, \omega)\}$ and $\mathrm{Re}\{\chi_0(\mathbf{q}, \omega)\}$. This hitherto unidentified unique origin of a CDW is enabled by near-linear dispersion of mono- and bilayer Te-*p* orbitals, which, because of favorable Fermi surface velocity (v_F), allows $\mathrm{Re}\{\chi_0(\mathbf{q}, \omega)\}$ and $\mathrm{Im}\{\chi_0(\mathbf{q}, \omega)\}$ to diverge at the same $\mathbf{q}_{CDW}$ from different Te-*p* orbitals. A critical implication of the divergence of $\mathrm{Re}\{\chi_0(\mathbf{q}, \omega)\}$ and $\mathrm{Im}\{\chi_0(\mathbf{q}, \omega)\}$ is the emergence of the Kohn anomaly in phonon dispersions [i.e., $\nabla_{\mathbf{q}} E(\mathbf{q}) \to \infty$] [32]. We calculate the imaginary part of $\chi_L(\mathbf{Q}, E)$, i.e., $\chi_L''(\mathbf{Q}, E)$, to show that indeed multiple phonon branches of both transverse and longitudinal polarizations harbor Kohn anomalies at $\mathbf{q}_{CDW}$ and unambiguously confirm that a CDW originates from a complex interplay of electron-hole pair formation in mono- and bilayer Te-*p* orbitals. Moreover, based on a detailed analysis of $\chi_0(\mathbf{q}, \omega)$ and $\chi_L(\mathbf{Q}, E)$, we provide focused input to control the CDW state, and we demonstrate it by selectively replacing Te monolayer atoms with another chalcogen atom.

I. CDW DISTORTION

Figure 1 shows the orthorhombic structure (*Pmmn*) of $EuTe_4$ in the unmodulated and CDW state. As mentioned earlier, EuTe layers are separated by one monolayer and one bilayer along the *c*-axis such that the stacking is (EuTe) − $\overline{\text{Te}}$ − $\overline{\text{Te}}$ − (EuTe) − $\underline{\text{Te}}$ − ⋯ [see Fig. 1(b)]. In the unmodulated state, mono- and bilayer Te atoms form a square-net pattern with a Te-Te bond distance of ∼3.23 Å [see the red and blue square in Fig. 1(a)], typical of hypervalent bonding that favors CDW distortion [16,18,33]. Te bilayers are separated by ∼3.37 Å with weak interlayer bonding, while Te in EuTe layer and Te in bilayers are ∼2.79 Å apart, thus forming a covalent bond. In the CDW state, Te atoms displace within the square-net to form a strong (shown as trimers in Fig. 1) and a weak (∼3.46 Å) bonding network. Te displacements are obtained from the freezing of unstable phonon eigenvector corresponding to a minimum energy configuration in a strongly anharmonic double-well potential (see supplementary Fig. S1 in the supplemental material [34]) and relaxation of atomic positions along an unstable phonon eigenvector within the framework of density functional theory (DFT). Both results show Te distortions along the experimentally determined CDW structure [16]. Notably, we observe that Te atoms in a bilayer have pronounced distortions as opposed to distortions in a monolayer [see the distortion of blue and red squares in Fig. 1(a)]. This difference in mono- and bilayer distortions has implications on the electronic band structure in the CDW state, as we discuss below.

II. ELECTRONIC BAND STRUCTURE AND ELECTRONIC SUSCEPTIBILITY

Figures 2(a) and (b) show the electronic band structure of $EuTe_4$ along high-symmetry directions. Simulations used the generalized gradient approximation (GGA) in the revised Perdew-Burke-Ernzerhof (PBE) parametrization [35] for solids with or without a Hubbard correction. Without a Hubbard correction, supplementary Fig. S2 shows a large EDOS from localized Eu-*f* states just below E_F. A large EDOS near E_F in high-symmetry structures with degenerate branches could induce lattice distortions by lifting symmetry restrictions and a lower overall system energy, as seen in several heavy actinides [28,29]. But a lack of degeneracy in the *Pmmn* spacegroup and an absence of spectral weight of *f* orbitals in ARPES measurements [17] suggest that *f* orbitals lie well below E_F. To treat the localized Eu-*f* electron states in GGA+*U* calculations, the total energy expression was described as introduced by Dudarev *et al.* [36] with on-site

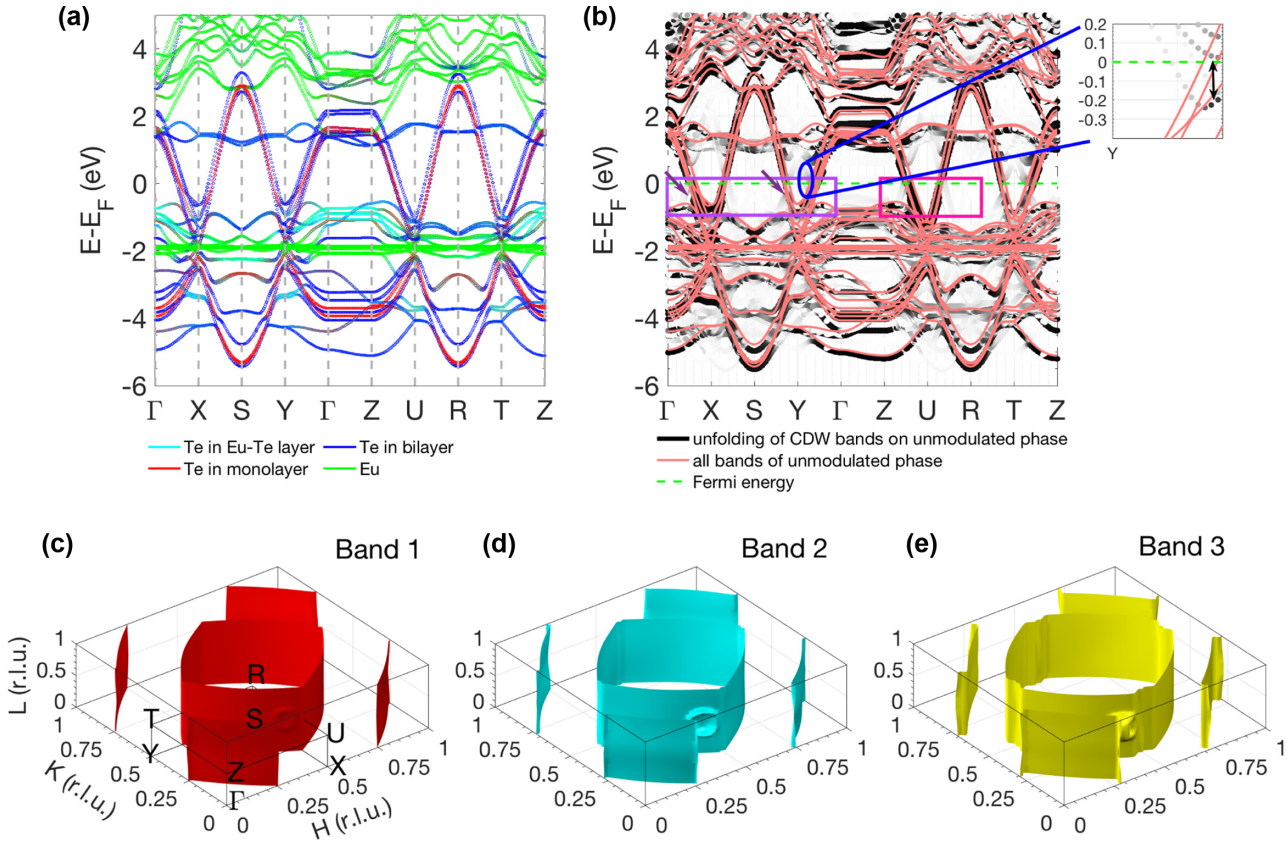

FIG. 2. (a) Atom-resolved band structure of unmodulated $EuTe_4$ highlighting the contribution of Eu atom and Te atoms in EuTe, Te bilayer, and Te monolayer, where the latter two occupy states across E_F. k-points are denoted in panel (c). (b) Band unfolding of CDW phase band on the unmodulated phase (black to white for decreasing contribution on linear scale between 1 and 0). Band-gap opening is evident from spectral weight loss for $L = 0$ (i.e., Γ-X-S-Y-Γ) at E_F, indicated by the purple rectangle and arrows. No weight loss is observed for $L = 0.5$ (i.e., Z-U-R) as shown within the pink rectangle. The inset shows the region near Y, indicated by the blue ellipse. The black double-arrow in the inset marks the band gap (∼0.2 eV). (c)–(e) Reconstruction of the Fermi surface in 3D from the three bands that cross E_F. The remaining three bands are shown in supplementary Fig. S11. Separate plots of the Fermi surface from different bands are for separating contributions from different Te atoms. r.l.u. refers to the reciprocal-lattice units.

Coulomb interaction varying between $U = 0$ and 7.0 eV. We find that up to $U = 2.5$ eV, f orbitals have a finite contribution at E_F. On further increasing U to 7 eV (used in subsequent simulations), localized Eu-f states shift further below E_F, while Te-p states and their Fermi surface topology remain unchanged (see supplementary Figs. S2, S5, S6, S8, S9, and S11).

In Fig. 2(a), we plot the contribution of Eu atoms and Te atoms from the monolayer, bilayer, and EuTe layer. We observe linear dispersion near E_F from Te-p orbitals of mono- and bilayers. The contribution of Te-p orbitals from the EuTe layer lies ∼1 eV below E_F. We further separate the Fermi surface from monolayer [band 2, Fig. 2(d)] and bilayer [bands 1 and 3, Figs. 2(c) and 2(e)] Te atoms. A detailed analysis of the atom- and orbital-resolved band structure and EDOS and the Fermi surface topology is provided in the supplemental material [34]. Parallel sheets of the Fermi surface are visible from Figs. 2(c)–2(e), which indicate a possibility of FSN and associated electronic instability leading to CDW formation. However, since sheets are not fully parallel (i.e., they are slightly curved), a detailed calculation of $\chi_0(\mathbf{q}, \omega)$ is necessary to determine $\mathbf{q}_{CDW}$ and its origin. Here $\chi_0(\mathbf{q}, \omega)$ is the electron-hole polarizability (also called the Lindhard response function) in the limit of adiabatic continuity, and it involves a calculation of electron-hole pair formation at $\mathbf{q}$ and ω weighted by the Fermi-Dirac function (see the supplemental material [34] for computational details).

Figure 3(a) shows Re$\{\chi_0(\mathbf{q})\}$ in the $(H, K, 0)$ reciprocal-lattice plane. We omit ω from $\chi_0(\mathbf{q}, \omega)$ when static polarizability is calculated, i.e., ω is zero. A twofold symmetry is visible as expected for the *Pmmn* structure. We observe several peaks; among them, the largest intensity peaks are along $[0, K, 0]$ as marked by black arrows at $K = 0.65$ and 0.35 r.l.u. Here r.l.u. refers to reciprocal-lattice units. Since the divergence of Re$\{\chi_0(\mathbf{q})\}$ governs the electronic instability [19,20,23], the peaks at $K = 0.35$ and 0.65 r.l.u. correspond to $\mathbf{q}_{CDW}$ of $EuTe_4$. Importantly, these peak positions are away from 2/3 and 1/3 r.l.u., thus they reflect an incommensurate modulation (also confirmed with the observation of multiple Kohn anomalies at $\mathbf{q}_{CDW}$, as shown later), which is consistent with recently measured $\mathbf{q}_{CDW} = (0, 0.643(3), 0)$ and 1-$\mathbf{q}_{CDW} = (0, 0.357(3), 0)$ r.l.u. using high-resolution single-crystal XRD [17]. Here we note that, similar to the RTe_3 family [9,14], because of the nearly square sheets within the

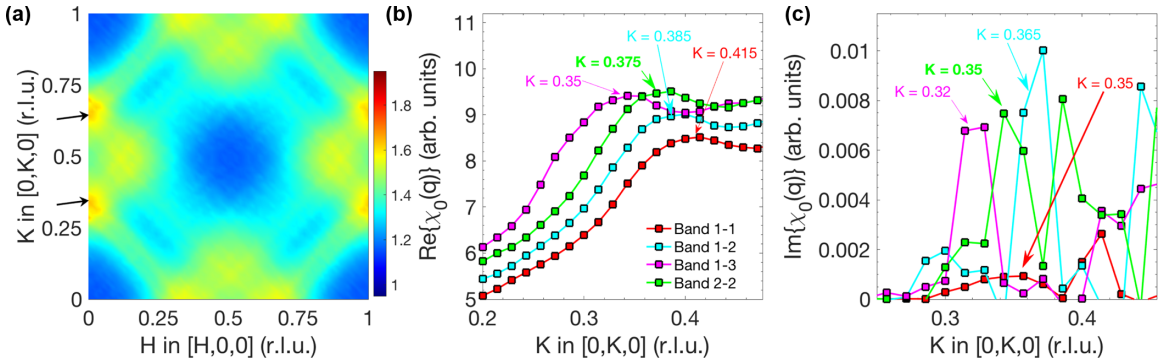

FIG. 3. (a) Re$\{\chi_0(\mathbf{q})\}$ of $EuTe_4$ in the $(H, K,0)$ plane. Colors represent the magnitude of Re$\{\chi_0(\mathbf{q})\}$ in arbitrary units. Black arrows mark the maximum value for $H = 0$. (b) Band-resolved Re$\{\chi_0(\mathbf{q})\}$ along $[0,K,0]$ (integrated over the L axis) from different combinations of bands. Fermi surfaces from different bands are shown in Fig. 2. Peak values of Re$\{\chi_0(\mathbf{q})\}$ are marked by arrows. (c) Same as panel (b), except for Im$\{\chi_0(\mathbf{q})\}$.

a-b plane, CDWs along the a and b axes compete in equilibrium. But as described in Ref. [9], the larger magnitude of Re$\{\chi_0(\mathbf{q})\}$ along K determines the initial $\mathbf{q}_{\mathrm{CDW}}$. Once the b-axis CDW forms, due to the change in the Fermi surface topology, i.e., the loss of states near E_{F}, the formation of an a-axis CDW is suppressed [9,14].

Such an excellent agreement of $\mathbf{q}_{\mathrm{CDW}}$ between experiments and simulations is reflective of high-density 3D Fermi surface sampling on a $70 \times 70 \times 70$ grid in the Brillouin zone (BZ) for calculation of the Fermi surface and Re$\{\chi_0(\mathbf{q})\}$. Consistent with experiments, $\mathbf{q}_{\mathrm{CDW}}$ does not change on varying the L index from 0 to 0.5 r.l.u. (see supplementary Fig. S14). To confirm the robustness of our results, we further repeated the simulations in the full BZ after including external perturbations at a given frequency $\omega = 12$ meV (i.e., perturbation from phonons), and we found that $\mathbf{q}_{\mathrm{CDW}}$ remains unchanged (see supplementary Figs. S15 and 22a). However, repeating the simulations with a shift in E_{F} by -50 and -75 meV did slightly change $\mathbf{q}_{\mathrm{CDW}}$ as expected due to shrinkage of the Fermi surface from linear dispersing bands (see supplementary Figs. S16, S17, and S22a). We emphasize that, since Re$\{\chi_0(\mathbf{q})\}$ is calculated in a first BZ for calculation, we obtain two first-order values of $|\mathbf{q}_{\mathrm{CDW}}| = 0.35$ and 0.65 r.l.u., which correspond to $(1 - \mathbf{q}_{\mathrm{CDW}})$ and $\mathbf{q}_{\mathrm{CDW}}$, respectively. We do not obtain any second-order $\mathbf{q}_{\mathrm{CDW}}$ measured in experiments as they originate from nesting in the band structure of the first and second BZ, but they can be calculated from $\mathbf{q}_{\mathrm{CDW}}$ of the first BZ, i.e., $2\mathbf{q}_{\mathrm{CDW}}$, 2-$2\mathbf{q}_{\mathrm{CDW}}$.

After confirming the magnitude and direction of $\mathbf{q}_{\mathrm{CDW}}$, we now focus on which bands contribute to the peak in Re$\{\chi_0(\mathbf{q})\}$ and Im$\{\chi_0(\mathbf{q})\}$. Divergent peaks in Im$\{\chi_0(\mathbf{q})\}$ and Re$\{\chi_0(\mathbf{q})\}$ correspond to FSN and the electronic instability wave vector (i.e., $\mathbf{q}_{\mathrm{CDW}}$), respectively [19,20,23]. If the same bands contribute to the divergence of both the real and imaginary parts, we can conclude that similar to the $R\mathrm{Te}_2$ [4,5] and $R\mathrm{Te}_3$ families [8], FSN governs CDW modulation. Figure 3(b) shows the contribution of different combinations of bands to Re$\{\chi_0(\mathbf{q})\}$ along $[0, K, 0]$ (i.e., electrons and holes reside on different bands). As one can observe, different combinations lead to peaks at different K values. In particular, we can observe that bands 1 and 3 lead to a peak at $\mathbf{q}_{\mathrm{CDW}}$ (magenta arrow at 0.35), while other bands contribute significantly away from $\mathbf{q}_{\mathrm{CDW}}$. On the other hand, we observe a pronounced peak in Im$\{\chi_0(\mathbf{q})\}$ at $\mathbf{q}_{\mathrm{CDW}}$ originating from the nesting of band 2 with itself [green, Fig. 3(c)], and other bands have a peak away from 0.35 r.l.u. Recall that band 2 originated from monolayer Te-p orbitals, while bands 1 and 3 are from bilayer Te-p orbitals. From the above orbital-resolved analysis, it is evident that the FSN wave vector [i.e., Im$\{\chi_0(\mathbf{q})\}$] and electronic instability [i.e., Re$\{\chi_0(\mathbf{q})\}$] have significant primary contributions from mono- and bilayer Te-p orbitals, respectively. Here we must emphasize two points. First, even though the peak in Re$\{\chi_0(\mathbf{q})\}$ at $\mathbf{q}_{\mathrm{CDW}}$ originates from bands 1 and 3, other bands, despite their peaks being away from $\mathbf{q}_{\mathrm{CDW}}$, also have a finite contribution at $\mathbf{q}_{\mathrm{CDW}}$. It is the sum of the contribution from all six bands that leads to the peak at $\mathbf{q}_{\mathrm{CDW}}$. Secondly, similar to previous studies [19,20], while the divergent behavior is not apparent at $\mathbf{q}_{\mathrm{CDW}}$ because of numerical approximations and the imperfect nesting wave vector [19], the curvature near $\mathbf{q}_{\mathrm{CDW}}$ shows divergence [see Fig. 3(b)].

The origin of orbital-dependent $\chi_0(\mathbf{q})$ lies in the linear dispersion of Te-p orbitals, which allows v_{F} to be constant in proximity to E_{F}. For calculation of Im$\{\chi_0(\mathbf{q})\}$, band energies are always restricted to the Fermi surface, i.e., $\epsilon_{\mathbf{k}} = \epsilon_{\mathbf{k}+\mathbf{q}} = E_{\mathrm{F}}$, while Re$\{\chi_0(\mathbf{q})\}$ includes contributions from bands above and below E_{F} [19]. A constant v_{F} in favorable conditions (i.e., $v_{\mathrm{F},\mathbf{k}} \simeq -v_{\mathrm{F},\mathbf{k}+\mathbf{q}}$) allows electron-hole pairs to form from bands present above and below the E_{F} at $\mathbf{q}_{\mathrm{CDW}}$ (i.e., $\epsilon_{\mathbf{k}} + v_{\mathrm{F},\mathbf{k}}\delta k$ and $\epsilon_{\mathbf{k}+\mathbf{q}} - v_{\mathrm{F},\mathbf{k}+\mathbf{q}}\delta k$), and consequently, as observed here, same pairs of bands lead to different peak locations in real and imaginary parts. Similar to our earlier study [23], we demonstrate the role of linearity by explicitly calculating k points and their relative contribution to Im$\{\chi_0(\mathbf{q})\}$ and Re$\{\chi_0(\mathbf{q})\}$. Figures 4(a) and 4(c) show k points from the entire 3D reciprocal lattice contributing to Im$\{\chi_0(\mathbf{q})\}$ at $K = 0.35$ arising from a combination of band 1–3. As one can notice, from the entire reciprocal lattice, only the k points lying on or close to the Fermi surface of band 1 [panel (a)] or 3 [panel (c)] contribute [overplotted on the Fermi surface for visualization; see also the inset for a 2D projection in the $(H, K, 0)$ plane]. Since at $K = 0.35$ no peak exists in Im$\{\chi_0(\mathbf{q})\}$ from a combination of bands 1–3 [see Fig. 3(c)], only a few k points contribute to it. On the other hand, as shown in Figs. 4(b) and 4(d), a considerably large number of k points contribute

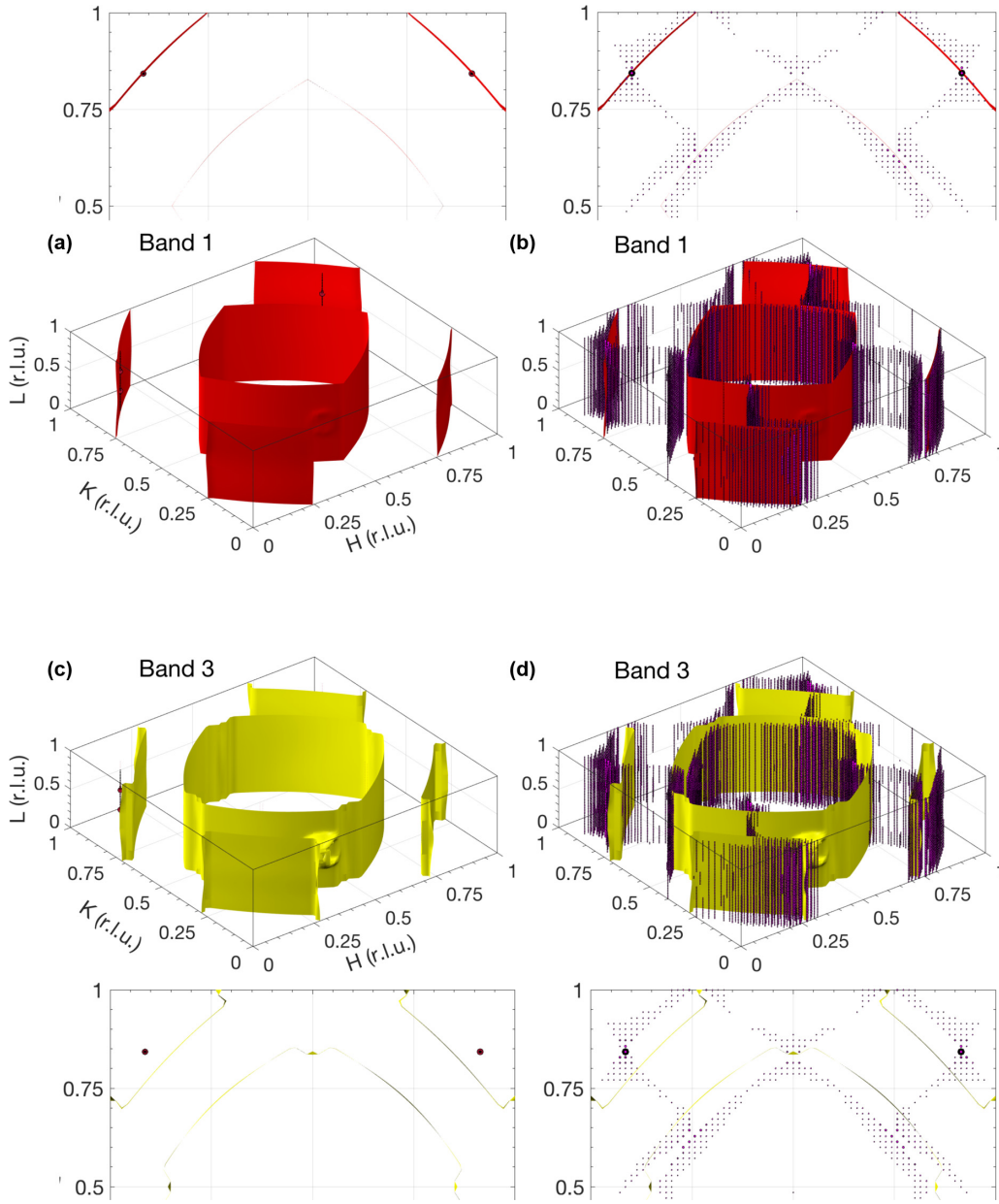

FIG. 4. (a), (c) k points from the entire 3D reciprocal lattice contributing to $\mathrm{Im}\{\chi_0(\mathbf{q})\}$ at $K = 0.35$ r.l.u. arising from a combination of bands 1–3 [see the magenta line in Fig. 3(c)]. From the entire reciprocal lattice, only the k points lying on or close to the Fermi surface of band 1 [panel (a)] or 3 [panel (c)] contribute; hence, they are overplotted on the Fermi surface for visualization. k points contributing up to 0.1% of the maximum value are displayed, with marker size indicating the relative contribution. The enlarged views on the top and bottom of panels (a) and (c) are a 2D projection in the $(H, K, 0)$ plane. (b), (d) Same as panels (a) and (c), but k points contributing to $\mathrm{Re}\{\chi_0(\mathbf{q})\}$ at $K = 0.35$ [see the magenta line in Fig. 3(b)]. k points contributing up to 2% of the maximum value are displayed, with marker size indicating the relative contribution. Because of the linearity of band dispersion and favorable v_F, parts of the Fermi surface and in-between that did not contribute to $\mathrm{Im}\{\chi_0(\mathbf{q})\}$ at $K = 0.35$ now have a finite contribution to $\mathrm{Re}\{\chi_0(\mathbf{q})\}$.

to the peak in $\mathrm{Re}\{\chi_0(\mathbf{q})\}$ at $K = 0.35$. Because of the linearity of band dispersion and favorable v_F, parts of the Fermi surface and in-between, which did not contribute to $\mathrm{Im}\{\chi_0(\mathbf{q})\}$ at $K = 0.35$, now have a finite contribution to $\mathrm{Re}\{\chi_0(\mathbf{q})\}$. However, as evident from the size of markers that indicate their relative contribution, k points farther from the Fermi surface contributes less due to the inverse square dependence on the energy difference between the electron and hole states.

Such atom-, orbital-, and momentum-resolved insights on the origin of a CDW allow us to engineer CDW states. In $EuTe_4$, since mono- and bilayers contribute differently to $\mathrm{Re}\{\chi_0(\mathbf{q})\}$ and $\mathrm{Im}\{\chi_0(\mathbf{q})\}$, we can tailor the CDW state by altering either of the layers. As shown in supplementary Figs. S27–S31, replacing monolayer Te with Se in $EuTe_4$ changes monolayer bands and Fermi surface topology; consequently, pronounced divergence in $\mathrm{Re}\{\chi_0(\mathbf{q})\}$ switches from the b- to

the a-axis (nearly equal maximum along both a- and b-axes, but marginally larger for the a-axis). Although we caution that in experiments (topological) defects and strain may also change $\mathbf{q}_{\mathrm{CDW}}$, as was recently observed for $LaTe_3$ [13,14] and $CeTe_2$ [37]. The CDW formation has implications on Te-p band renormalization and the electronic band gap, as we discuss below.

III. CDW BAND GAP

We calculated the electronic bands of the CDW state after relaxing the atomic coordinates along the direction of CDW distortion in a $1 \times 3 \times 1$ supercell of the unmodulated structure [the relaxed structure is shown in Fig. 1(a)]. Although the modulation is incommensurate, we find the supercell size to be adequate to capture the key features of band renormalization. We unfolded the supercell bands on unmodulated unit cells to directly compare the CDW and unmodulated bands [38–41]. Figure 2(b) shows the contribution of unfolded bands as intensity (white to black for increasing contribution), which are overplotted with the bands of unmodulated structure (red). As one can see, Te-p bands are strongly renormalized at E_{F} leading to a band-gap opening of ∼0.2 eV (see the purple rectangle; arrows mark the reduced intensity, and the inset shows the band-gap magnitude), consistent with an observed band gap of 0.19–0.24 eV from ARPES measurements in the $(H, K, 0)$ plane [17]. However, we note that the band gap is not fully opened at the $L = 0.5$ r.l.u. plane (Z-U-R direction) as denoted by the pink rectangle. This is because we did not include any CDW modulation along the z-axis (see supplementary Fig. S26a) as they have not been experimentally confirmed by observation of superlattice peaks or electrical resistivity measurements along the c-axis [16,17]. Moreover, as discussed earlier, since structural relaxation and phonon eigenvectors found monolayer Te distortions to be relatively less compared to bilayer Te distortions, we see relatively small remnant intensity near E_{F} from monolayer Te-p orbitals (not immediately visible by the naked eye in the purple rectangle). It is possible to remove the residual intensity by freezing monolayer Te distortion at $\mathbf{q} = (0, 1/3, 0)$ r.l.u. (see supplementary Fig. S26b), but such distortions need to be experimentally confirmed before their incorporation in simulations.

IV. LATTICE SUSCEPTIBILITY

As observed for several CDW compounds, CDW signatures are visible in phonons, albeit differently for different governing mechanisms [42,43]. To unequivocally confirm CDW instability in $EuTe_4$, we calculate phonon dispersion within the harmonic approximation. As shown in Fig. 5(a), we observe an unstable phonon branch at $\mathbf{q}_{\mathrm{CDW}}$ along Γ-Y, consistent with divergence of $\mathrm{Re}\{\chi_0(\mathbf{q})\}$ and $\mathrm{Im}\{\chi_0(\mathbf{q})\}$. Displacement of atoms corresponding to the eigenvector of an unstable phonon is shown in Fig. 1(a), which is the same as the relaxed atomic coordinates of the CDW state and XRD data [16], thus confirming that the unstable phonon indeed reflects CDW instability. This instability is stabilized in our anharmonic simulations at 800 K, which explicitly capture the effect of coupling between atomic vibrations and electronic states at finite temperature (see supplementary Fig. S25). The stabilization at 800 K is consistent with the reported mean-field T_{CDW} of ∼646 K [17]. Moreover, as expected, the signatures of incipient CDW instability are even visible at $\mathbf{q}_{\mathrm{CDW}}$ at 800 K.

Besides the dominant phonon instability, following the seminal work of Kohn [32], divergence of $F(\mathbf{q}) \propto \mathrm{Re}\{\chi_0(\mathbf{q})\}/|\mathbf{q}|^2$ must lead to Kohn anomalies [i.e., $\nabla_{\mathbf{q}} E(\mathbf{q}) \rightarrow \infty$] in multiple phonon branches. This is because $F(\mathbf{q})$ affects electron screening for $\mathbf{q} > \mathbf{q}_{\mathrm{CDW}}$, and alters the restoring interatomic forces. The sudden change in interatomic forces perturbs multiple branches at $\mathbf{q}_{\mathrm{CDW}}$, which involves the displacement of atoms contributing to the divergence of $F(\mathbf{q})$. We calculate the imaginary part of lattice dynamical susceptibility, i.e., $\chi_L''(\mathbf{Q}, E)$, to show unambiguously that indeed multiple phonon branches of both transverse and longitudinal polarizations harbor Kohn anomalies at $\mathbf{q}_{\mathrm{CDW}}$ [see the supplemental material [34] for details of $\chi_L''(\mathbf{Q}, E)$ simulations].

Figure 5(b) shows $\chi_L''(\mathbf{Q}, E)$ along $[2, K, 0]$ selectively highlighting transverse polarization for $K \leqslant 1$ (i.e., a-polarized phonons propagating along K). Between $1 < K \leqslant 2$, we obtain a mixture of transverse and longitudinal polarization. We have marked Kohn anomalies in different phonon branches at $\mathbf{q}_{\mathrm{CDW}}$. As one can observe, not only the unstable phonon branch (the lowest branch going below zero meV) but also high-energy branches that involve displacement of Te mono- and bilayer show anomalous features instead of a smooth dispersion at $\mathbf{q}_{\mathrm{CDW}}$. Similarly, we probe the pure longitudinal polarization (i.e., b-polarized phonons propagating along K) and another transverse polarization (i.e., c-polarized phonons propagating along K) in Figs. 5(c) and 5(d). More Kohn anomalies at $\mathbf{q}_{\mathrm{CDW}}$ in multiple branches are marked by white arrows. We note that $\chi_L''(\mathbf{Q}, E)$ is shown in different BZs for varying polarizations as anomalous features appear in those BZs with measurable intensity; nonetheless, data can be folded back to the first BZ. From the above phonon dispersions and $\chi_L''(\mathbf{Q}, E)$ analysis, we confirm signatures of CDW instability in multiple phonon branches at $\mathbf{q}_{\mathrm{CDW}}$ as expected from the divergence of $\mathrm{Re}\{\chi_0(\mathbf{q})\}$ and recently shown for α-U [23]. The appearance of multiple Kohn anomalies at $\mathbf{q}_{\mathrm{CDW}}$ further excludes the wave-vector-dependent EPI mechanism proposed for $NbSe_2$, $TbTe_3$, and $DyTe_3$ [11,12,24,25]. This is because, for the wave-vector-dependent EPI, the scattering of an electron to another state by absorption or emission of a phonon conserves the energy and momentum [44,45]. However, this conservation is unlikely to be satisfied for multiple phonon branches simultaneously at a fixed $\mathbf{q}_{\mathrm{CDW}}$ [23,45]. Hence, we do not observe a Kohn anomaly for multiple branches at $\mathbf{q}_{\mathrm{CDW}}$, rather we observe it for a particular branch [11,12,23–25].

In summary, using our atom-, momentum-, and orbital-resolved analysis of $\chi_0(\mathbf{q})$, we find that the FSN and electronic instability leading to CDW do not arise from the same Te orbitals and are rather primarily driven by Te orbitals of monolayers and bilayers, respectively. This unique behavior is enabled by linear dispersion of Te-p orbitals across E_{F} that allows v_{F} to be nearly constant and electron-hole pairs to form from bands above and below E_{F}, thus contributing to the divergence of $\mathrm{Re}\{\chi_0(\mathbf{q})\}$ and the emergence of multiple Kohn anomalies at $\mathbf{q}_{\mathrm{CDW}}$. The detailed analysis presented here is not limited to the $R\mathrm{Te}_n$ family, but is equally applicable to

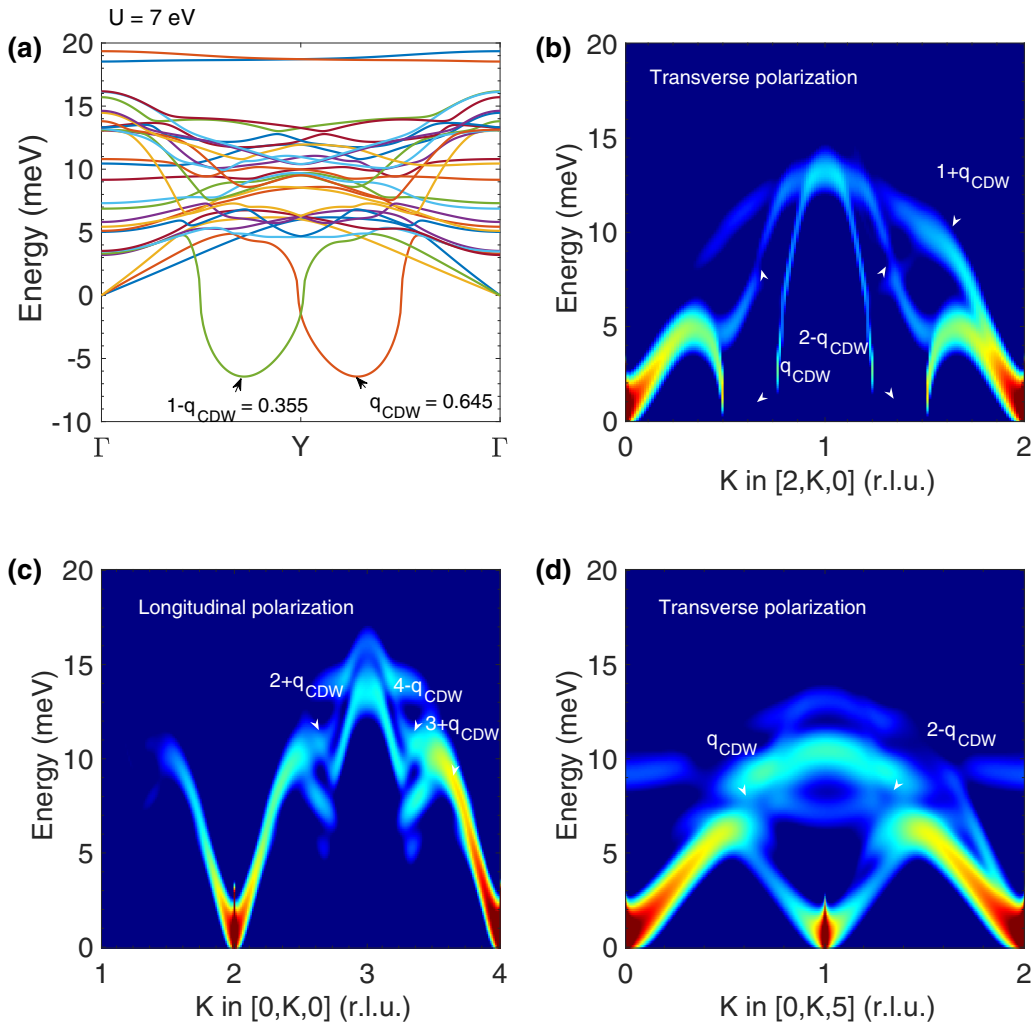

FIG. 5. (a) Phonon dispersions of $EuTe_4$ along the Γ-Y-Γ direction showing the phonon instabilities at $\mathbf{q}_{\mathrm{CDW}}$ as marked by arrows. (b) $\chi_L''(\mathbf{Q}, E)$ along the $[2, K, 0]$ direction selectively highlighting the a-polarized transverse branches for $K \leqslant 1$. For $1 < K \leqslant 2$, we obtain components of both transverse and longitudinal branches. (c) Same as panel (b), except the intensity originates from b-polarized longitudinal branches. (d) Same as panel (b), except the intensity originates from c-polarized transverse branches for $K \leqslant 1$. For $1 < K \leqslant 2$, we obtain components of both transverse and longitudinal branches. The intensity is in log scale spanning five decades and indicates the magnitude of $\chi_L''(\mathbf{Q}, E)$.

recently observed axionic CDWs [46,47], spin-density waves (SDWs) [48], and Kohn anomalies [49,50] from *ubiquitous* linearly dispersing bands in topological Weyl/Dirac semimetals. More generally, our study provides focused input for atom and orbital engineering to tailor CDW and SDW transitions, topological phase transitions [50], superconducting kagome metals [51], and possibly phase transition in high-T superconductors wherein a precursor CDW or a charge-ordering state is present [42,43,52–55].

ACKNOWLEDGMENTS

We thank N. L. Wang for providing us cif files of $EuTe_4$. D.B. gratefully acknowledges the financial support from BRNS-DAE under Project No. 58/14/30/2019-BRNS/11117, and MoE/STARS under Project No. MoE/STARS-1/345. The simulations were performed at the SPACETIME-II supercomputing facility at IITB and the ANUPAM supercomputing facility at BARC.

[1] G. Grüner, *Density Waves in Solids* (Addison-Wesley, Reading, MA, 1994)

[2] M. Dressel and G. Gruner, *Electrodynamics of Solids: Optical Properties of Electrons in Matter* (Cambridge University Press, Cambridge, 2002).

[3] K. Shin, V. Brouet, N. Ru, Z. Shen, and I. Fisher, Phys. Rev. B **72**, 085132 (2005).

[4] D. Garcia, G.-H. Gweon, S. Zhou, J. Graf, C. Jozwiak, M. Jung, Y. Kwon, and A. Lanzara, Phys. Rev. Lett. **98**, 166403 (2007).

[5] E. Lee, D. Kim, J. Denlinger, J. Kim, K. Kim, B. Min, B. Min, Y. Kwon, and J.-S. Kang, Phys. Rev. B **91**, 125137 (2015).

[6] C. Malliakas, S. J. Billinge, H. J. Kim, and M. G. Kanatzidis, J. Am. Chem. Soc. **127**, 6510 (2005).

[7] V. Brouet, W. Yang, X. Zhou, Z. Hussain, N. Ru, K. Shin, I. Fisher, and Z. Shen, Phys. Rev. Lett. **93**, 126405 (2004).

[8] V. Brouet, W. Yang, X. Zhou, Z. Hussain, R. Moore, R. He, D. Lu, Z. Shen, J. Laverock, S. Dugdale, N. Ru, and I. Fisher, Phys. Rev. B **77**, 235104 (2008).

[9] N. Ru, C. Condron, G. Margulis, K. Shin, J. Laverock, S. Dugdale, M. Toney, and I. Fisher, Phys. Rev. B **77**, 035114 (2008).

[10] G.-H. Gweon, J. Denlinger, J. Clack, J. Allen, C. Olson, E. DiMasi, M. Aronson, B. Foran, and S. Lee, Phys. Rev. Lett. **81**, 886 (1998).

[11] M. Maschek, S. Rosenkranz, R. Heid, A. Said, P. Giraldo-Gallo, I. Fisher, and F. Weber, Phys. Rev. B **91**, 235146 (2015).

[12] M. Maschek, D. Zocco, S. Rosenkranz, R. Heid, A. Said, A. Alatas, P. Walmsley, I. Fisher, and F. Weber, Phys. Rev. B **98**, 094304 (2018).

[13] A. Zong, A. Kogar, Y.-Q. Bie, T. Rohwer, C. Lee, E. Baldini, E. Ergeçen, M. B. Yilmaz, B. Freelon, E. J. Sie *et al.*, Nat. Phys. **15**, 27 (2019).

[14] A. Kogar, A. Zong, P. E. Dolgirev, X. Shen, J. Straquadine, Y.-Q. Bie, X. Wang, T. Rohwer, I.-C. Tung, Y. Yang, R. Li, J. Yang, S. Weathersby, S. Park, M. E. Kozina, E. J. Sie, H. Wen, P. Jarillo-Herrero, I. R. Fisher, X. Wang *et al.*, Nat. Phys. **16**, 159 (2020).

[15] S. Seong, E. Lee, Y. S. Kwon, B. I. Min, J. D. Denlinger, B.-G. Park, and J. Kang, Electron. Struct. **3**, 024003 (2021).

[16] D. Wu, Q. Liu, S. Chen, G. Zhong, J. Su, L. Shi, L. Tong, G. Xu, P. Gao, and N. Wang, Phys. Rev. Mater. **3**, 024002 (2019).

[17] B. Lv, A. Zong, D. Wu, A. Rozhkov, B. V. Fine, S.-D. Chen, M. Hashimoto, D.-H. Lu, M. Li, Y.-B. Huang *et al.*, arXiv:2106.09774.

[18] W. Tremel and R. Hoffmann, J. Am. Chem. Soc. **109**, 124 (1987).

[19] M. Johannes and I. Mazin, Phys. Rev. B **77**, 165135 (2008).

[20] X. Zhu, Y. Cao, J. Zhang, E. Plummer, and J. Guo, Proc. Natl. Acad. Sci. (USA) **112**, 2367 (2015).

[21] X. Zhu, J. Guo, J. Zhang, and E. Plummer, Adv. Phys.: X **2**, 622 (2017).

[22] M.-H. Whangbo, E. Canadell, P. Foury, and J.-P. Pouget, Science **252**, 96 (1991).

[23] A. P. Roy, N. Bajaj, R. Mittal, P. D. Babu, and D. Bansal, Phys. Rev. Lett. **126**, 096401 (2021).

[24] F. Weber, S. Rosenkranz, J.-P. Castellan, R. Osborn, R. Hott, R. Heid, K.-P. Bohnen, T. Egami, A. Said, and D. Reznik, Phys. Rev. Lett. **107**, 107403 (2011).

[25] F. Weber, R. Hott, R. Heid, K.-P. Bohnen, S. Rosenkranz, J.-P. Castellan, R. Osborn, A. Said, B. Leu, and D. Reznik, Phys. Rev. B **87**, 245111 (2013).

[26] C.-W. Chen, J. Choe, and E. Morosan, Rep. Prog. Phys. **79**, 084505 (2016).

[27] S. Gerber, H. Jang, H. Nojiri, S. Matsuzawa, H. Yasumura, D. Bonn, R. Liang, W. Hardy, Z. Islam, A. Mehta *et al.*, Science **350**, 949 (2015).

[28] A. Boring and J. Smith, Los Alamos Sci. **26**, 90 (2000).

[29] P. Söderlind, A. Landa, and B. Sadigh, Adv. Phys. **68**, 1 (2019).

[30] R. Peierls, *Quantum Theory of Solids* (Oxford University Press, New York, 1955).

[31] R. Peierls, *More Surprises in Theoretical Physics* (Princeton University Press, Princeton, NJ, 1991).

[32] W. Kohn, Phys. Rev. Lett. **2**, 393 (1959).

[33] G. A. Papoian and R. Hoffmann, Angew. Chem. Int. Ed. **39**, 2408 (2000).

[34] See Supplemental Material at http://link.aps.org/supplemental/10.1103/PhysRevB.105.035120 for computational details and supplementary figures.

[35] G. I. Csonka, J. P. Perdew, A. Ruzsinszky, P. H. Philipsen, S. Lebègue, J. Paier, O. A. Vydrov, and J. G. Ángyán, Phys. Rev. B **79**, 155107 (2009).

[36] S. Dudarev, G. Botton, S. Savrasov, C. Humphreys, and A. Sutton, Phys. Rev. B **57**, 1505 (1998).

[37] B. Sharma, M. Singh, B. Ahmed, B. Yu, P. Walmsley, I. R. Fisher, and M. C. Boyer, Phys. Rev. B **101**, 245423 (2020).

[38] T. B. Boykin and G. Klimeck, Phys. Rev. B **71**, 115215 (2005).

[39] T. B. Boykin, N. Kharche, G. Klimeck, and M. Korkusinski, J. Phys.: Condens. Matter **19**, 036203 (2007).

[40] P. B. Allen, T. Berlijn, D. Casavant, and J. M. Soler, Phys. Rev. B **87**, 085322 (2013).

[41] U. Herath, P. Tavadze, X. He, E. Bousquet, S. Singh, F. Muoz, and A. H. Romero, Comput. Phys. Commun. **251**, 107080 (2020).

[42] G. Ghiringhelli, M. Le Tacon, M. Minola, S. Blanco-Canosa, C. Mazzoli, N. Brookes, G. De Luca, A. Frano, D. Hawthorn, F. He *et al.*, Science **337**, 821 (2012).

[43] M. Le Tacon, A. Bosak, S. M. Souliou, G. Dellea, T. Loew, R. Heid, K.-P. Bohnen, G. Ghiringhelli, M. Krisch, and B. Keimer, Nat. Phys. **10**, 52 (2014).

[44] G. Grimvall, *The Electron-phonon Interaction in Metals* (North-Holland, Amsterdam, 1981).

[45] F. Giustino, Rev. Mod. Phys. **89**, 015003 (2017).

[46] J. Gooth, B. Bradlyn, S. Honnali, C. Schindler, N. Kumar, J. Noky, Y. Qi, C. Shekhar, Y. Sun, Z. Wang, B. A. Bernevig, and C. Felser, Nature (London) **575**, 315 (2019).

[47] W. Shi, B. J. Wieder, H. L. Meyerheim, Y. Sun, Y. Zhang, Y. Li, L. Shen, Y. Qi, L. Yang, J. Jena, P. Werner, K. Koepernik, S. Parkin, Y. Chen, C. Felser, B. A. Bernevig, and Z. Wang, Nat. Phys. **17**, 381 (2021).

[48] J. Gaudet, H.-Y. Yang, S. Baidya, B. Lu, G. Xu, Y. Zhao, J. A. Rodriguez-Rivera, C. M. Hoffmann, D. E. Graf, D. H. Torchinsky, P. Nikolic, D. Vanderbilt, F. Tafti, and C. L. Broholm, Nat. Mater. **20**, 1650 (2021).

[49] T. Nguyen, F. Han, N. Andrejevic, R. Pablo-Pedro, A. Apte, Y. Tsurimaki, Z. Ding, K. Zhang, A. Alatas, E. E. Alp *et al.*, Phys. Rev. Lett. **124**, 236401 (2020).

[50] S. Yue, B. Deng, Y. Liu, Y. Quan, R. Yang, and B. Liao, Phys. Rev. B **102**, 235428 (2020).

[51] H. Tan, Y. Liu, Z. Wang, and B. Yan, Phys. Rev. Lett. **127**, 046401 (2021).

[52] D. Reznik, L. Pintschovius, M. Ito, S. Iikubo, M. Sato, H. Goka, M. Fujita, K. Yamada, G. Gu, and J. Tranquada, Nature (London) **440**, 1170 (2006).

[53] J. Hamlin, D. Zocco, T. Sayles, M. Maple, J.-H. Chu, and I. Fisher, Phys. Rev. Lett. **102**, 177002 (2009).

[54] R. Comin, A. Frano, M. M. Yee, Y. Yoshida, H. Eisaki, E. Schierle, E. Weschke, R. Sutarto, F. He, A. Soumyanarayanan *et al.*, Science **343**, 390 (2014).

[55] S. Lee, G. De La Penã, S. X.-L. Sun, M. Mitrano, Y. Fang, H. Jang, J.-S. Lee, C. Eckberg, D. Campbell, J. Collini, J. Paglione, F. M. F. de Groot, and P. Abbamonte, Phys. Rev. Lett. **122**, 147601 (2019).